

Michelson–Morley analogue for electrons using trapped ions to test Lorentz symmetry

T. Pruttivarasin^{1,2}, M. Ramm¹, S. G. Porsev^{3,4}, I. I. Tupitsyn⁵, M. S. Safronova^{3,6}, M. A. Hohensee^{1,7} & H. Häffner¹

All evidence so far suggests that the absolute spatial orientation of an experiment never affects its outcome. This is reflected in the standard model of particle physics by requiring all particles and fields to be invariant under Lorentz transformations. The best-known tests of this important cornerstone of physics are Michelson–Morley-type experiments verifying the isotropy of the speed of light^{1–3}. For matter, Hughes–Drever-type experiments^{4–11} test whether the kinetic energy of particles is independent of the direction of their velocity, that is, whether their dispersion relations are isotropic. To provide more guidance for physics beyond the standard model, refined experimental verifications of Lorentz symmetry are desirable. Here we search for violation of Lorentz symmetry for electrons by performing an electronic analogue of a Michelson–Morley experiment. We split an electron wave packet bound inside a calcium ion into two parts with different orientations and recombine them after a time evolution of 95 milliseconds. As the Earth rotates, the absolute spatial orientation of the two parts of the wave packet changes, and anisotropies in the electron dispersion will modify the phase of the interference signal. To remove noise, we prepare a pair of calcium ions in a superposition of two decoherence-free states, thereby rejecting magnetic field fluctuations common to both ions¹². After a 23-hour measurement, we find a limit of $h \times 11$ millihertz (h is Planck's constant) on the energy variations, verifying the isotropy of the electron's dispersion relation at the level of one part in 10^{18} , a 100-fold improvement on previous work⁹. Alternatively, we can interpret our result as testing the rotational invariance of the Coulomb potential. Assuming that Lorentz symmetry holds for electrons and that the photon dispersion relation governs the Coulomb force, we obtain a fivefold-improved limit on anisotropies in the speed of light^{2,3}. Our result probes Lorentz symmetry violation at levels comparable to the ratio between the electroweak and Planck energy scales¹³. Our experiment demonstrates the potential of quantum information techniques in the search for physics beyond the standard model.

Invariance under Lorentz transformations is a key feature of the standard model, and as such is fundamental to nearly every aspect of modern physics. Nevertheless, this symmetry may be measurably violated, for example, as a result of spontaneous symmetry breaking in quantum fields with dynamics at experimentally inaccessible energy scales not explicitly treated by the standard model¹⁴. Some theories that unify gravitation and the standard model assert that Lorentz symmetry is valid only at large length scales^{15,16}. A natural estimate of the fractional shift of electron dispersion relations due to Lorentz violation at the Planck scale is given by the ratio between the electroweak and Planck energy scales, that is, $\sim 2 \times 10^{-17}$ (ref. 13). Other models suggest that large Lorentz violation at the Planck scale is suppressed by supersymmetry¹⁷. In such scenarios, the constraints on Lorentz violation for neutrons⁶ can be used to set an upper bound of order 100 TeV on the supersymmetric energy scale¹⁸. Therefore, precision tests of Lorentz symmetry complement

direct probes of high-energy physics being carried out at the Large Hadron Collider.

We analyse Lorentz violation in the context of a phenomenological framework known as the standard model extension^{19,20} (SME). The SME is an effective field theory that augments the standard model Lagrangian with every possible combination of the standard model fields that is not term-by-term Lorentz invariant, while maintaining gauge invariance, energy–momentum conservation, and Lorentz invariance of the total action^{19,20}. The SME can be used to describe the low-energy limit of many different theories which predict Lorentz violation, and includes the standard model as a limiting case. The SME thus provides a comprehensive framework for quantifying a wide range of Lorentz-violating effects, and is a flexible tool for consistently evaluating a wide variety of experiments²¹.

The SME allows for Lorentz violation for all particles separately. However, to verify a particle's Lorentz symmetry, it must be compared with a reference system because only differences in their behaviours under Lorentz transformation are observable²⁰. For instance, typical interpretations of Michelson–Morley experiments testing Lorentz violation of photons assume that the lengths of the interferometer arms are invariant under rotations. Because the lengths of interatomic bonds depend on the electron dispersion relation^{22,23}, those interpretations can be said to assume that Lorentz symmetry for electrons (and nuclei making up the interferometer arms) holds unless a second distinct reference system is used²³. For our experiment, it seems more natural to use light as a reference and assume that photons obey Lorentz symmetry. However, it is important to keep in mind that an experimental signature of the Lorentz violation considered here can equally be attributed to Lorentz violation of electrons as well as to that of photons, which would manifest itself as an asymmetry of the photon-mediated Coulomb potential (Methods). Thus, we take the most general view, namely that we measure the difference between the electron and photon anisotropies.

We take this view by choosing a coordinate system in which a hypothetical Lorentz violation in light manifests itself in the electronic Lagrangian (Methods). We obtain the modified electronic quantum electrodynamics Lagrangian

$$\mathcal{L} = \frac{1}{2} i \bar{\psi} \left(\gamma_\nu + c'_{\mu\nu} \gamma^\mu \right) \bar{D}^\nu \psi - \bar{\psi} m_e \psi \quad (1)$$

where m_e is the electron mass, ψ is a Dirac spinor, γ^μ are the Dirac matrices and $\bar{\psi} \bar{D}^\nu \psi \equiv \bar{\psi} D^\nu \psi - \psi D^\nu \bar{\psi}$ with D^ν being the covariant derivative. The effect due to Lorentz violation is described by the tensor $c'_{\mu\nu} = c_{\mu\nu} + k_{\mu\nu}/2$, which contains Lorentz-violation parameters from both the electron ($c_{\mu\nu}$) and the photon ($k_{\mu\nu}$) sectors^{19,20}. Because $c'_{\mu\nu}$ is frame dependent, we uniquely specify its value in the Sun-centred, celestial-equatorial frame (SCCEF), that is, the Sun's rest frame. Time-dependent Lorentz transformations due to the Earth's motion transform $c'_{\mu\nu}$ in the SCCEF to the time-dependent values in the local laboratory frame

¹Department of Physics, University of California, Berkeley, California 94720, USA. ²Quantum Metrology Laboratory, RIKEN, Wako, Saitama 351-0198, Japan. ³Department of Physics and Astronomy, University of Delaware, Newark, Delaware 19716, USA. ⁴Petersburg Nuclear Physics Institute, Gatchina, Leningrad District 188300, Russia. ⁵Department of Physics, St Petersburg State University, Ulianovskaya 1, Petrodvorets, St Petersburg 198504, Russia. ⁶Joint Quantum Institute, National Institute of Standards and Technology and the University of Maryland, College Park, Maryland 20742, USA. ⁷Lawrence Livermore National Laboratory, Livermore, California 94550, USA.

on the Earth. Hence, the contribution of $c'_{\mu\nu}$ to any laboratory-frame observable will vary in time.

For us, the important consequence of electronic Lorentz violation is the dependence of an electron's energy on the direction of its momentum. For an atomically bound electron with momentum \mathbf{p} , the Lagrangian in equation (1) results in a small energy shift that depends on the direction of the electron's momentum and is described by the effective Hamiltonian²⁴

$$\delta\mathcal{H} = -C_0^{(2)} \frac{(\mathbf{p}^2 - 3p_z^2)}{6m_e} \quad (2)$$

where $C_0^{(2)}$ contains elements in $c'_{\mu\nu}$ in the laboratory frame and p_z is the component of the electron's momentum along the quantization axis, which is fixed in the laboratory. The energy shift depends on how the total momentum \mathbf{p} is distributed among the three spatial components. As the Earth rotates, $C_0^{(2)}$ varies in time, resulting in a time variation of the electron's energy correlated with the Earth's motion.

To probe Lorentz violation, we perform the electronic analogue of a Michelson–Morley experiment by interfering atomic states with anisotropic electron momentum distributions aligned along different directions, such as available in the $^2D_{5/2}$ manifold of $^{40}\text{Ca}^+$. We trap a pair of $^{40}\text{Ca}^+$ ions with an ion–ion separation of $\sim 16\ \mu\text{m}$ in a linear Paul trap, and define the quantization axis by applying a static magnetic field of 3.930 G vertically. The direction of this magnetic field changes with respect to the Sun as the Earth rotates, resulting in a rotation of our interferometer (Fig. 1).

We calculate the Lorentz-violation-induced hypothetical energy shift of $^{40}\text{Ca}^+$ in the $^2D_{5/2}$ manifold according to equation (2) (expressed here in hertz):

$$\frac{\Delta E}{h} = [(2.16 \times 10^{15}) - (7.42 \times 10^{14})m_J]C_0^{(2)}$$

where m_J is the magnetic quantum number (Methods). To obtain maximum sensitivity to Lorentz violation, we monitor the energy difference between the states $|\pm 5/2\rangle \equiv |^2D_{5/2}; m_J = \pm 5/2\rangle$ and $|\pm 1/2\rangle \equiv |^2D_{5/2}; m_J = \pm 1/2\rangle$ using a Ramsey-type interferometric scheme. To reject magnetic field noise, which is the main source of decoherence, we create a product state $|\Psi^P\rangle = (1/2)(|-1/2\rangle + |-5/2\rangle) \otimes (|+1/2\rangle + |+5/2\rangle)$ by applying to both ions a series of $\pi/2$ - and π -pulses on

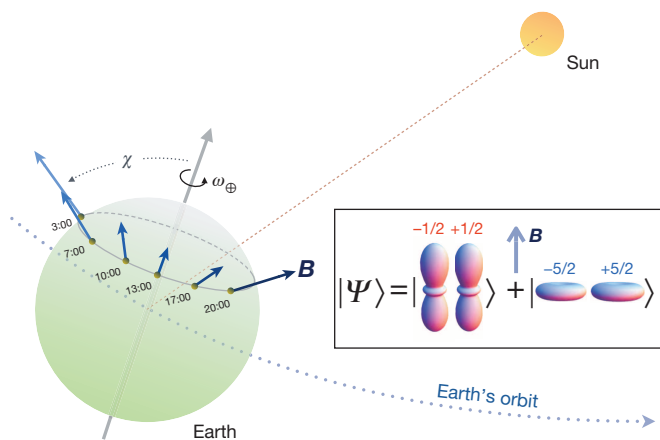


Figure 1 | Rotation of the quantization axis of the experiment with respect to the Sun as the Earth rotates. We apply a magnetic field (B) of 3.930 G vertically in the laboratory frame to define the quantization axis of the experiment. As the Earth rotates with an angular frequency given by $\omega_{\oplus} = 2\pi/(23.93\ \text{h})$, the orientation of the quantization axis and, consequently, that of the electron wave packet (as shown in the inset in terms of probability envelopes) changes with respect to the Sun's rest frame (positions at various times UTC are illustrated). The angle $\chi \approx 52.1^\circ$ is the colatitude of the experiment.

the $S_{1/2}$ – $D_{5/2}$ transition. Under common noise induced by a fluctuating magnetic field, the product state rapidly dephases to a mixed state that contains a decoherence-free entangled state $|\Psi^R\rangle \equiv (1/\sqrt{2})(|-5/2, +5/2\rangle + |-1/2, +1/2\rangle)$ with 50% probability²⁵. This entangled state evolves freely in time according to

$$|\Psi^R(t)\rangle = \frac{1}{\sqrt{2}}(|-5/2, +5/2\rangle + e^{i(\Delta E_R t/h + \phi_R)}|-1/2, +1/2\rangle)$$

where ΔE_R is the energy difference between the states $|-5/2, +5/2\rangle$ and $|-1/2, +1/2\rangle$, ϕ_R is a phase offset and \hbar is Planck's constant divided by 2π . The remaining components of the mixed state, which are the states $|-5/2, +1/2\rangle$ and $|-1/2, +5/2\rangle$, each with 25% probability, are time independent.

In Fig. 2, we illustrate the dynamics of the state $|\Psi^R\rangle$. By expressing the state in the even–odd parity basis, $|\pm\rangle = (1/\sqrt{2})(|-5/2, +5/2\rangle \pm |-1/2, +1/2\rangle)$, the time-dependent state can be written as

$$|\Psi^R(t)\rangle = \frac{1}{\sqrt{2}}\left(\left(1 + e^{i(\Delta E_R t/h + \phi_R)}\right)|+\rangle + \left(1 - e^{i(\Delta E_R t/h + \phi_R)}\right)|-\rangle\right) \quad (3)$$

We interpret the trajectory of $|\Psi^R(t)\rangle$ to be along the equator of the Bloch sphere as shown in Fig. 2b. The state $|\Psi^R(t)\rangle$ oscillates back and forth between the states $|+\rangle$ and $|-\rangle$ with frequency $f_R = \Delta E_R/h$. To read out the ion state in the $|\pm\rangle$ basis, we apply to both ions a series of π - and $\pi/2$ -pulses on the $S_{1/2}$ – $D_{5/2}$ transition, followed by an electron-shelving readout scheme¹². The difference between the probabilities

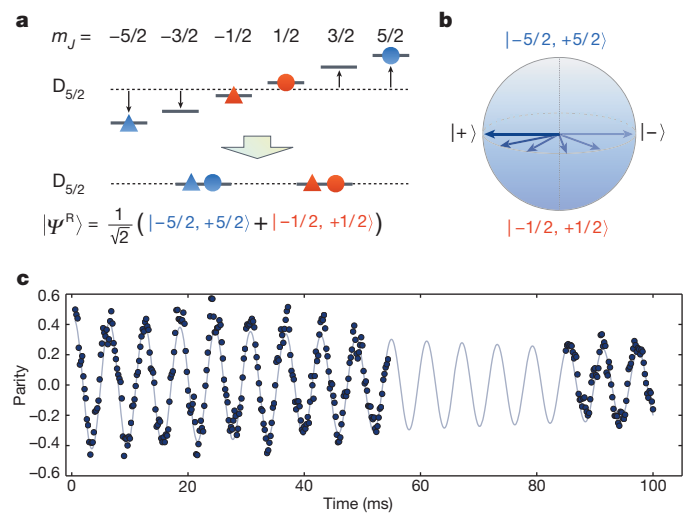


Figure 2 | Oscillation of the decoherence-free state. **a**, A combination of different magnetic sublevels of the first (circles) and second (triangles) $^{40}\text{Ca}^+$ ions in the $^2D_{5/2}$ manifold forms a decoherence-free state $|\Psi^R\rangle \equiv (1/\sqrt{2})(|-5/2, +5/2\rangle + |-1/2, +1/2\rangle)$. Blue and red colours indicate pairing of the single-ion states in each component of $|\Psi^R\rangle$. **b**, Time evolution of the state $|\Psi^R(t)\rangle$ represented by a trajectory on a Bloch sphere with poles given by $|-5/2, +5/2\rangle$ and $|-1/2, +1/2\rangle$. (We neglected contributions from the states $|-5/2, +1/2\rangle$ and $|-1/2, +5/2\rangle$, which have no phase coherence.) The state $|\Psi^R(t)\rangle$ oscillates back and forth between the even–odd parity basis states, $|\pm\rangle$, as given in equation (3). **c**, Oscillation of a product state containing an entangled state $|\Psi^R\rangle$ with 50% probability. Each data point is derived from 200 repetitions of the Ramsey-type experimental cycle shown in Fig. 3a. The error bars (no larger than data symbols, and omitted to simplify figure) are obtained from requiring that the fit to the Ramsey fringe function (grey solid line) gives $\sqrt{\chi^2_{\text{reduced}}} = 1$ and assuming that the data are normally distributed. The fit yields an oscillation frequency of $164.9 \pm 0.1\ \text{Hz}$ and a decay constant of $155 \pm 17\ \text{ms}$, which is substantially smaller than the value expected from the lifetime of the $^2D_{5/2}$ state of $^{40}\text{Ca}^+$. We attribute the loss of coherence to the heating rate of the ion trap, of $\sim 0.2\ \text{quanta ms}^{-1}$, which degrades the quality of the analysis pulses for long Ramsey interrogation times. To save measurement time, data was not taken in the ~ 60 – $80\ \text{ms}$ interval.

P_+ and P_- of the ions being in the states $|+\rangle$ and $|-\rangle$, respectively, yields an oscillating signal given by $P = P_+ - P_- = \cos(\Delta E_R t / \hbar + \phi_R)$ (Fig. 2c).

We are interested in the variations in the energy difference between the $|\pm 5/2, \mp 5/2\rangle$ and $|\pm 1/2, \mp 1/2\rangle$ states due to Lorentz violation. However, the energy difference is also affected by linear Zeeman shifts from a residual magnetic field gradient, quadratic Zeeman shifts, electric quadrupole shifts from an electric field gradient, and a.c. Stark shifts from oscillating trapping fields^{26,27}. The contributions from the magnetic field gradient, which are of order 100 Hz, have opposite signs for the state $|\Psi^R\rangle$ and its mirrored counterpart, $|\Psi^L\rangle \equiv (1/\sqrt{2})(|+5/2, -5/2\rangle + |+1/2, -1/2\rangle)$. We can subtract out the contribution from the magnetic field gradient to the oscillation signal by taking the average frequency $\bar{f} = (f_R + f_L)/2$, where f_R and f_L are the oscillation frequencies of state $|\Psi^R\rangle$ and $|\Psi^L\rangle$, respectively (Extended Data Fig. 1). The remaining effects (except for Lorentz violation) are energy shifts of order of only a few hertz and are also directly related to external electromagnetic fields in the proximity of the ions. We expect these fields to

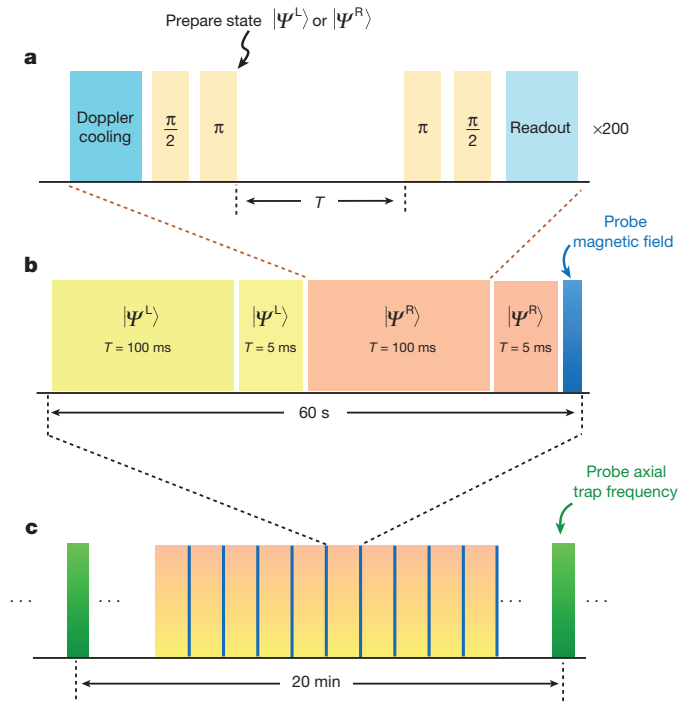


Figure 3 | Outline of the experimental scheme. **a**, The building blocks of our experiment are Ramsey-type interferometric sequences. In each measurement cycle, we first perform Doppler cooling and optical pumping of the ions. Then a series of $\pi/2$ - and π -pulses on the $S_{1/2}$ – $D_{5/2}$ transition prepare the ions in a product state that dephases into a mixed state within 1 ms. This state contains an entangled state $|\Psi^{L,R}\rangle \equiv (1/\sqrt{2})(|+5/2, \mp 5/2\rangle + |\pm 1/2, \mp 1/2\rangle)$ with 50% probability. Afterwards, the mixed state evolves freely for Ramsey duration T , before another series of π - and $\pi/2$ -pulses, together with an electron-shelving readout sequence, allows us to read out the state of the ions in the even–odd parity basis. This measurement cycle is repeated 200 times each for $|\Psi^L\rangle$ and $|\Psi^R\rangle$. **b**, To correct for phase drifts in the preparation of $|\Psi^{L,R}\rangle$, we measure the difference in the oscillation signal between Ramsey durations of 100 and 5 ms. We then correct for the contribution of the magnetic field gradient by taking the average of the oscillation signals measured with states $|\Psi^L\rangle$ and $|\Psi^R\rangle$. At the end of this measurement block, we measure the magnetic field by performing spectroscopy on the $S_{1/2}$ – $D_{5/2}$ transition to correct for the quadratic Zeeman effect. Each grey data point in Fig. 4a is a result from one of these measurement blocks. **c**, We continuously repeat the measurement block during the course of the 23 h-long measurement. To correct for the electric quadrupole shift caused by the electric field gradient, we measure the axial trap frequency by performing spectroscopy on the $S_{1/2}$ – $D_{5/2}$ transition.

be stable on the 10^{-3} level over the course of a day, and the associated variations are on the level of a few millihertz and below. Moreover, we independently measure these fields using the ions themselves as a probe (Methods).

We measured the energy difference between the states $|\pm 5/2, \mp 5/2\rangle$ and $|\pm 1/2, \mp 1/2\rangle$ of $^{40}\text{Ca}^+$ for 23 h starting from 3:00 coordinated universal time (UTC) on 19th April 2014, by monitoring the oscillation signal of the ions with an effective Ramsey duration of 95 ms (Methods). At the same time, we monitored the magnetic field and the electric field gradient using the ions themselves as a probe (Fig. 3). We then used the measured values of the magnetic field and electric field gradient to correct for the quadratic Zeeman and electric quadrupole shifts. The resulting 23 h frequency measurement is shown in Fig. 4. With 23 h of averaging, we reach a sensitivity of the oscillation frequency of 11 mHz, limited by statistical uncertainties due to short-term fluctuations. We then attribute any residual variation in the energy correlated with the Earth’s rotation to Lorentz violation.

Lorentz transformations of ζ'_{uv} from the SCCEF to the laboratory frame results in the time-dependent energy shift due to Lorentz violation given by

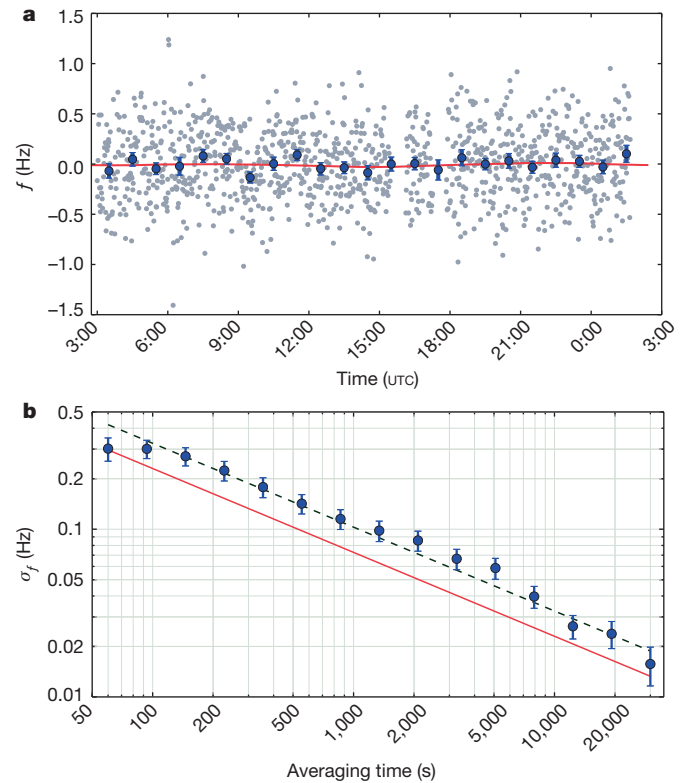


Figure 4 | Frequency measurements for $^{40}\text{Ca}^+$. **a**, The grey data points represent frequency measurements of $^{40}\text{Ca}^+$ taken after each measurement block as shown in Fig. 3b, with contributions from the quadratic Zeeman shifts and electric quadrupole shifts subtracted out. (Gaps in the data points are due to a failure of the laser frequency stabilization.) We started the measurement at 3:00 UTC on 19 April 2014, and continued for 23 h. The blue points are obtained by binning of data from 60 min time intervals. The error bars represent 1 s.d. of the data points within the bin, where we scale the error by $\sqrt{\chi^2_{\text{reduced}}}/N = 1.3$ (obtained from the fit of the binned data to the model in equation (4)). **b**, The blue points show the Allan deviation of the frequency measurement, σ_f , calculated from the unbinned data with error bars representing 1 s.d. The red solid line is the estimated quantum projection noise. The green dashed line is a fit to the data, showing a sensitivity to the ions’ energy variation of $\sigma_t = 3.3 \text{ Hz}/\sqrt{\tau}$, where τ is the averaging time. The steady downward trend indicates that we are still limited by statistical fluctuations rather than by correlated noise or systematics over the course of the measurement.

Table 1 | Limits on differential electron–photon Lorentz-violation parameters $c'_{\mu\nu} = c_{\mu\nu} + k_{\mu\nu}/2$

Parameters ($c'_{\mu\nu} = c_{\mu\nu} + k_{\mu\nu}/2$)	New limits	Existing limits	
		$c_{\mu\nu}$ (electrons)	$k_{\mu\nu}/2$ (photons)
$-0.16c'_{X-Y} + 0.33c'_{XY} - 0.92c'_{XZ} - 0.16c'_{YZ}$	$0.1 \pm 1.0 \times 10^{-18}$	$-0.9 \pm 1.0 \times 10^{-16}$	$-2.5 \pm 3.5 \times 10^{-18}$
$-0.04c'_{X-Y} - 0.32c'_{XY} - 0.35c'_{XZ} + 0.88c'_{YZ}$	$2.4 \pm 7.4 \times 10^{-19}$	$-0.9 \pm 6.5 \times 10^{-17}$	$-5.2 \pm 3.6 \times 10^{-18}$
$0.29c'_{X-Y} - 0.38c'_{XY} - 0.73c'_{XZ} - 0.48c'_{YZ}$	$5.9 \pm 9.5 \times 10^{-19}$	$-8.1 \pm 9.5 \times 10^{-17}$	$-0.6 \pm 3.8 \times 10^{-18}$
$-0.31c'_{X-Y} - 0.65c'_{XY} + 0.07c'_{XZ} - 0.69c'_{YZ}$	$0.7 \pm 1.2 \times 10^{-18}$	$-2.9 \pm 6.5 \times 10^{-17}$	$-2.6 \pm 3.8 \times 10^{-18}$

Fitting our frequency measurements to the model in equation (4) yields the limits on Lorentz-violation parameters $c'_{\mu\nu}$ in the SCCEF. All uncertainties for the uncorrelated combinations of $c'_{\mu\nu}$ are 1 s.d. from the fit conservatively scaled with $\langle\chi^2_{\text{reduced}}\rangle = 1.3$. We improve the bounds from ref. 9 on the electron dispersion by up to two orders of magnitude. Alternatively, we can work in coordinates such that the electron dispersion is isotropic. We then improve by up to five times on the existing limits for the isotropy of the speed of light set by a modern version of the classic Michelson–Morley experiment in ref. 2 (Methods). Note that the work in ref. 9 assumed that $k_{\mu\nu} = 0$ whereas that in ref. 2 assumed that $c_{\mu\nu} = 0$. We use the notation $c'_{X-Y} = c'_{XX} - c'_{YY}$.

$$\frac{\Delta E}{h} = A \cos(\omega_{\oplus} T) + B \sin(\omega_{\oplus} T) + C \cos(2\omega_{\oplus} T) + D \sin(2\omega_{\oplus} T) \quad (4)$$

where $\omega_{\oplus} = 2\pi/(23.93 \text{ h})$ is the sidereal angular frequency of the Earth's rotation, T is the time since the vernal equinox of 2014, and A, B, C and D are parameters related to $c'_{\mu\nu}$ in the SCCEF (Methods). Fitting our data (Fig. 4) to equation (4) yields the limits of the $c'_{\mu\nu}$ parameters, which we report and compare with existing limits in Table 1. We improve the best measurements for those parameters, carried out by precision spectroscopy of dysprosium⁹, by up to two orders of magnitude, to a level of 10^{-18} . Alternatively, we can assume that Lorentz symmetry holds for electrons. We then can interpret our results as limits on Lorentz violation for photons (Methods) and improve on the bounds for Lorentz symmetry set by photon Michelson–Morley experiments² by up to five times (Table 1).

Our experimental scheme is readily applicable to other trapped-ion species considered for quantum information purposes. Many of those possess a long-lived electronic state with a non-vanishing angular momentum. Thus, further improvement can be achieved by increasing the Ramsey durations using metastable states with significantly longer lifetimes, such as 30 s for the barium ion²⁸, or by using ions more sensitive to Lorentz violation, such as highly charged ions²⁹. Additionally, by preparing a pure entangled state of the ions instead of a mixed state, it is possible to gain another factor of two in signal-to-noise ratio¹². Finally, we do not see any signature of limiting systematic effects, and thus expect that future extensions of our experimental technique with better statistics will yield tests of Lorentz symmetry at the level of 10^{-20} and below, where the polarization of black-body radiation in combination with temperature changes is expected to become relevant.

Online Content Methods, along with any additional Extended Data display items and Source Data, are available in the online version of the paper; references unique to these sections appear only in the online paper.

Received 25 August; accepted 12 November 2014.

- Michelson, A. A. & Morley, E. W. On the relative motion of the Earth and the luminiferous ether. *Am. J. Sci.* **34**, 333–345 (1887).
- Herrmann, S. *et al.* Rotating optical cavity experiment testing Lorentz invariance at the 10^{-17} level. *Phys. Rev. D* **80**, 105011 (2009).
- Eisele, Ch., Nevsky, A. Yu. & Schiller, S. Laboratory test of the isotropy of light propagation at the 10^{-17} level. *Phys. Rev. Lett.* **103**, 090401 (2009).
- Hughes, V. W., Robinson, H. G. & Beltran-Lopez, V. Upper limit for the anisotropy of inertial mass from nuclear resonance experiments. *Phys. Rev. Lett.* **4**, 342–344 (1960).
- Drever, R. W. P. A search for anisotropy of inertial mass using a free precession technique. *Phil. Mag.* **6**, 683–687 (1961).
- Smicklas, M., Brown, J. M., Cheuk, L. W., Smullin, S. J. & Romalis, M. V. New test of local Lorentz invariance using a ^{21}Ne -Rb-K comagnetometer. *Phys. Rev. Lett.* **107**, 171604 (2011).
- Allmendinger, F. *et al.* Upper limit for the anisotropy of inertial mass from nuclear resonance experiments. *Phys. Rev. Lett.* **112**, 110801 (2014).
- Peck, S. K. *et al.* Upper limit for the anisotropy of inertial mass from nuclear resonance experiments. *Phys. Rev. A* **86**, 012109 (2012).

- Hohensee, M. A. *et al.* Limits on violations of Lorentz symmetry and the Einstein equivalence principle using radio-frequency spectroscopy of atomic dysprosium. *Phys. Rev. Lett.* **111**, 050401 (2013).
- Altschul, B. Testing electron boost invariance with 2S–1S hydrogen spectroscopy. *Phys. Rev. D* **81**, 041701(R) (2010).
- Matveev, A. *et al.* Precision measurement of the hydrogen 1S–2S frequency via a 920-km fiber link. *Phys. Rev. Lett.* **110**, 230801 (2013).
- Roos, C. F., Chwalla, M., Kim, K., Riebe, M. & Blatt, R. 'Designer atoms' for quantum metrology. *Nature* **443**, 316–319 (2006).
- Kostecký, V. A. & Potting, R. CPT, strings, and meson factories. *Phys. Rev. D* **51**, 3923–3935 (1995).
- Kostecký, V. A. & Samuel, S. Spontaneous breaking of Lorentz symmetry in string theory. *Phys. Rev. D* **39**, 683–685 (1989).
- Hořava, P. Quantum gravity at a Lifshitz point. *Phys. Rev. D* **79**, 084008 (2009).
- Pospelov, M. & Shang, Y. Lorentz violation in Horava-Lifshitz-type theories. *Phys. Rev. D* **85**, 105001 (2012).
- Nibbelink, S. G. & Pospelov, M. Lorentz violation in supersymmetric field theories. *Phys. Rev. Lett.* **94**, 081601 (2005).
- Liberati, S. & Mattingly, D. Lorentz breaking effective field theory models for matter and gravity: theory and observational constraints. Preprint at <http://arxiv.org/abs/1208.1071> (2012).
- Colladay, D. & Kostelecký, V. A. CPT violation and the standard model. *Phys. Rev. D* **55**, 6760–6774 (1997).
- Colladay, D. & Kostelecký, V. A. Lorentz-violating extension of the standard model. *Phys. Rev. D* **58**, 116002 (1998).
- Russell, N. & Kostelecký, V. A. Data tables for Lorentz and CPT violation. *Rev. Mod. Phys.* **83**, 11–31 (2011).
- Müller, H., Herrmann, S., Saenz, A., Peters, A. & Lämmerzahl, C. Optical cavity tests of Lorentz invariance for the electrons. *Phys. Rev. D* **68**, 116006 (2003).
- Müller, H. Testing Lorentz invariance by the use of vacuum and matter filled cavity resonators. *Phys. Rev. D* **71**, 045004 (2005).
- Kostecký, V. A. & Lane, C. Constraints on Lorentz violation from clock-comparison experiments. *Phys. Rev. D* **60**, 116010 (1999).
- Chwalla, M. *et al.* Precision spectroscopy with two correlated atoms. *Appl. Phys. B* **89**, 483–488 (2007).
- Chou, C. W., Hume, D. B., Rosenband, T. & Wineland, D. J. Optical clocks and relativity. *Science* **329**, 1630–1633 (2010).
- Madej, A., Dubé, P., Zhou, Z., Bernard, J. E. & Gertsulov, M. $^{88}\text{Sr}^+$ 445-THz single-ion reference at the 10^{-17} level via control and cancellation of systematic uncertainties and its measurement against the SI second. *Phys. Rev. Lett.* **109**, 203002 (2012).
- Iskrenova-Tchoukova, E. & Safronova, M. S. Theoretical study of lifetimes and polarizabilities in Ba^+ . *Phys. Rev. A* **78**, 012508 (2008).
- Safronova, M. S. *et al.* Highly-charged ions for atomic clocks, quantum information, and search for α -variation. *Phys. Rev. Lett.* **113**, 030801 (2014).

Acknowledgements This work was supported by the NSF CAREER programme grant no. PHY 0955650 and NSF grants no. PHY 1212442 and no. PHY 1404156, and was performed under the auspices of the US Department of Energy by Lawrence Livermore National Laboratory under contract DE-AC52-07NA27344. We thank H. Müller for critical reading of the manuscript.

Author Contributions H.H., M.A.H. and T.P. had the idea for the experiment. T.P. and M.R. carried out the measurements. S.G.P., I.I.T. and M.S.S. calculated the sensitivity of the energy to Lorentz violation. T.P., M.A.H. and H.H. wrote the main part of the manuscript. S.G.P., I.I.T. and M.S.S. wrote the Methods section on calculating the energy shift. All authors contributed to the discussions of the results and manuscript.

Author Information Reprints and permissions information is available at www.nature.com/reprints. The authors declare no competing financial interests. Readers are welcome to comment on the online version of the paper. Correspondence and requests for materials should be addressed to T.P. (thaned.prutivrasin@riken.jp) or H.H. (hhaeffner@berkeley.edu).

METHODS

Lorentz-violation parameters of electrons and photons. While Lorentz symmetry, or local Lorentz invariance, requires that the laws of physics be the same in all coordinate systems in the group formed by Lorentz transformations, it does not restrict our initial choice of coordinates. As a result, some forms of Lorentz violation cannot be unambiguously attributed to a single species of elementary particle without first specifying this coordinate choice. In particular, we can select our initial coordinates such that $c_{\mu\nu}$ (or its gauge field analogue $k_{\mu\nu}$) vanishes at leading order for any single species of particle (or gauge field). This particle then becomes a Lorentz-covariant ‘yardstick’ which other species can be compared against. For instance one might use light as the yardstick; that is, one would measure space such that $x_i = c_i t$ with the speed of light c_i constant in all three spatial directions i . Alternatively, one might use a coordinate system for which Lorentz symmetry is preserved for electrons. Then the value of $c_i t$ might not be the same in all three spatial directions. In this case Lorentz violation would manifest itself by breaking the rotational symmetry of the photon-mediated Coulomb force, yielding the same measurable energy shift as in the previous case. Consequently, a single experimental approach typically constrains a linear combination of particles and gauge fields.

To analyse which linear combination in the SME we test in our experiment, we neglect contributions of the nucleus to the Lorentz-violation signal for two reasons. First, the quadrupole moment of the doubly magic $^{40}\text{Ca}^+$ nucleus is expected to vanish. Second, the violations of Lorentz symmetry for nucleon constituents have been constrained to 10^{-26} for protons³⁰ and 10^{-29} for neutrons^{6,7}. In addition to the Lorentz-violating Lagrangian for electrons (equation (1)) in the SME, the Lorentz violation for electromagnetic fields (photons) is given by the parameters \tilde{k}^{JK} ($J, K = X, Y, Z$) (which are functions of $k_{\mu\nu}$) in the Lagrangian³¹

$$\mathcal{L} = \frac{1}{2} \left[(1 + \tilde{k}_{\text{tr}}) |\mathbf{E}|^2 - (1 - \tilde{k}_{\text{tr}}) |\mathbf{B}|^2 \right] + \frac{1}{2} [\mathbf{E} \tilde{\mathbf{k}}_{e-} \mathbf{E} - \mathbf{B} \tilde{\mathbf{k}}_{e-} \mathbf{B}] + \mathbf{E} \tilde{\mathbf{k}}_{o+} \mathbf{B} \quad (5)$$

where \tilde{k}_{tr} is a scalar, $\tilde{\mathbf{k}}_{e-}$ is a 3×3 traceless symmetric matrix that characterizes the anisotropy of the speed of light, and $\tilde{\mathbf{k}}_{o+}$ is a 3×3 antisymmetric matrix. By means of a coordinate transformation, observation of Lorentz violation for both the electrons and photons can be made to appear only in either the SME Lagrangian for the electron sector (equation (1)) or the photon sector (equation (5)). In both cases, the linear combinations of parameters relevant to our experiment are³²

$$\begin{aligned} c'_{X-Y} &= c_{XX} - c_{YY} + \frac{1}{2} (\tilde{k}_{e-}^{XX} - \tilde{k}_{e-}^{YY}) \\ c'_{XY} &= c_{XY} + \frac{1}{2} \tilde{k}_{e-}^{XY} \\ c'_{XZ} &= c_{XZ} + \frac{1}{2} \tilde{k}_{e-}^{XZ} \\ c'_{YZ} &= c_{YZ} + \frac{1}{2} \tilde{k}_{e-}^{YZ} \end{aligned}$$

The best existing limits on \tilde{k}_{e-}^{XY} , \tilde{k}_{e-}^{XZ} , \tilde{k}_{e-}^{YZ} and $\tilde{k}_{e-}^{XX} - \tilde{k}_{e-}^{YY}$ are given in ref. 2. In Table 1, we compare our results to these limits.

Experimental set-up. We trap a pair of $^{40}\text{Ca}^+$ ions in a linear Paul trap with an interelectrode distance of 1.0 mm. We apply a radio-frequency with peak-to-peak voltage of ~ 500 V to each pair of the radio-frequency electrodes. One pair of the electrodes is driven in antiphase with the other pair. With a ~ 4 V d.c. voltage applied across the end caps, we obtain trap frequencies of $2\pi \times (2.2, 2.0)$ MHz in the radial directions and $2\pi \times 210$ kHz in the axial direction. The axial direction is aligned horizontally in the laboratory frame. To define a quantization axis, we apply a static magnetic field of 3.930 G vertically (at 45° with respect to both radial directions of the trap) using a coil. Additionally, we use another magnetic coil to compensate for residual magnetic field gradient along the axial direction.

Two independent 729 nm laser beams in the vertical direction drive π - and $\pi/2$ -pulses on the $S_{1/2}$ - $D_{5/2}$ transition on each ion separately. Both beams are derived from a laser stabilized to a high-finesse optical cavity to better than 100 Hz. Another beam path addressing both ions in the horizontal direction (at 45° with respect to the axial direction) is used for Doppler cooling (397 nm and 866 nm) and repumping the $D_{5/2}$ state (854 nm). We perform all laser light switching and frequency shifting using acousto-optical modulators (AOMs) in a double-pass configuration. We generate all radio-frequency voltages supplied to the AOMs using direct-digital-synthesizer chips from Analogue Devices (AD9910). The timing in the experimental sequence is controlled by a field-programmable gate-array (FPGA) module (XEM6010) from Opal Kelly. We characterize the stability of the on-board crystal oscillator using a frequency counter (Agilent 53210A). The clock stability is measured to be at the level of 4×10^{-7} , which translates to better than 5 μHz stability in the oscillation signal of the measurement of Lorentz violation.

Measurement scheme. The experimental sequence is shown in Fig. 3. We measure four independent oscillation signals for the two states $|\Psi^L\rangle \equiv (1/\sqrt{2})(|+5/2, -5/2\rangle + |-1/2, -1/2\rangle)$ and $|\Psi^R\rangle \equiv (1/\sqrt{2})(|-5/2, +5/2\rangle + |-1/2, +1/2\rangle)$, each with both short ($T_{\text{short}} = 5$ ms) and long ($T_{\text{long}} = 100$ ms) Ramsey duration (Fig. 3b). Within each measurement block in Fig. 3b, the order in which we perform Ramsey spectroscopy for each state and the Ramsey duration is randomized to average out systematic noise that might coincide with the period (~ 60 s) of the measurement block.

In general, the oscillation signal has the form $S(t) = \mathcal{A} \cos(2\pi f t + \phi_{\text{offset}} + \phi_{\text{laser}}) + \mathcal{B}$, where \mathcal{A} is the amplitude of the signal, \mathcal{B} is a possible offset to the overall level of the signal, f is the oscillation frequency, ϕ_{offset} is the phase offset and ϕ_{laser} is an additional phase that we can control by changing the phase of the 729 nm laser (using the radio-frequency signal supplied to the AOM for each beam path) that drives π - and $\pi/2$ -pulses on the $S_{1/2}$ - $D_{5/2}$ transition of the ions.

For a given state and Ramsey duration, the Ramsey interferometric cycle shown in Fig. 3a is repeated 200 times. To cancel out drifts in the offset of the signal, \mathcal{B} , we perform the first 100 cycles of the Ramsey sequence with the phase of the laser given by ϕ_{laser} and the next 100 cycles with the phase of the laser given by $\phi_{\text{laser}} + \pi$. We then calculate the difference between these two signals, $(S(\phi_{\text{laser}}) - S(\phi_{\text{laser}} + \pi))/2 = \mathcal{A} \cos(2\pi f t + \phi_{\text{offset}} + \phi_{\text{laser}})$, which does not depend on \mathcal{B} .

For a fixed Ramsey duration T , the oscillation signal $S(T) = \mathcal{A} \cos(2\pi f T + \phi_{\text{offset}} + \phi_{\text{laser}})$ is most sensitive to variation in the oscillation frequency, f , when the signal crosses zero, that is, when $2\pi f T + \phi_{\text{offset}} + \phi_{\text{laser}} = \pi/2$. We make sure that the oscillation signal remains close to zero by adding the phase correction calculated from the oscillation signal, that is, $\delta\phi = \cos^{-1}(S(T)/\mathcal{A}) - \pi/2$, to the phase of the laser light, ϕ_{laser} . The long-term measurement of the variation in the oscillation frequency, δf , is then derived from the phase correction data using $\delta\phi = 2\pi T \delta f$.

In addition to the change in the oscillation frequency, any change in ϕ_{offset} in the state preparation affects the phase correction: $\delta\phi = 2\pi T \delta f + \delta\phi_{\text{offset}}$. To correct for a contribution from this phase offset, we use signals from the two Ramsey durations ($T_{\text{short}} = 5$ ms and $T_{\text{long}} = 100$ ms) and calculate the difference between the phase corrections: $\delta\phi_{\text{long}} - \delta\phi_{\text{short}} = 2\pi(T_{\text{long}} - T_{\text{short}})\delta f$. The oscillation frequency for the state $|\Psi^{L,R}\rangle$ is given by $\delta f_{L,R} = [(\delta\phi_{\text{long}} - \delta\phi_{\text{short}})/2\pi(T_{\text{long}} - T_{\text{short}})]_{L,R}$, where the effective Ramsey duration is $T_{\text{long}} - T_{\text{short}} = 95$ ms.

Whereas the linear Zeeman effects from a magnetic field common to both ions drops out, the linear Zeeman effect due to a magnetic field gradient does not. In a typical unshielded laboratory environment, the gradient remains stable enough to allow for contrast with Ramsey times of about 30 s (ref. 33). To remove extant frequency variations from the gradient, we take the average frequency $\delta\bar{f} = (\delta f_L + \delta f_R)/2$ (Extended Data Fig. 1), which now contains only contributions from the electric quadrupole shift, the quadratic Zeeman shift, a.c. Stark shifts from oscillating trapping fields, and shifts from Lorentz violation.

We characterize the effect of the electric quadrupole shift by measuring the oscillation frequency $\delta\bar{f}$ as a function of the electric field gradient by changing the axial trap frequency. For our experimental set-up, we obtain $\delta\bar{f} = 4.0(8)$ (Hz mm² V⁻¹) $E' + 8.9(8)$ (Hz), where E' is the electric field gradient. At our operating axial trap frequency of 210 kHz, this translates to variations in the quadrupole shift due to changes in the axial trap frequency of 27 ± 12 mHz kHz⁻¹. The offset of 8.9(8) Hz is due to the quadratic Zeeman shift, which agrees with the estimated value of 8 Hz for the applied magnetic field of 3.930 G. Any change in the magnitude of the applied magnetic field near our operating value of 3.930 G gives a variation of the quadratic Zeeman shift of 4 mHz mG⁻¹. Using the ions as a probe, we measure both the magnetic field and the axial trap frequency during the course of the experiment and correct for their contributions to the oscillation signal. Over the course of our 23 h-long run, our axial trap frequency varies by less than ~ 1 kHz and the magnetic field by less than 1 mG. These instabilities translate into variations in the correction to the oscillation frequency of ~ 30 mHz, due to the quadrupole shift, and 3 mHz, due to the magnetic field. Fitting the model in equation (4) to the corrections only, we find that not taking into account the axial frequency instability would cause a false Lorentz-violation signal with amplitudes of less than 3 mHz, and that not correcting for the magnetic field instabilities would cause a signal with amplitudes of less than 0.5 mHz. Thus, in principle no correction for their drift would have been necessary. We note also that by measuring those quantities during the measurement run, their average contributions are expected to decrease as fast as the primary measurement signal, and should thus pose no limitation on improved Lorentz symmetry tests with longer measurement runs.

The oscillating electric field from the radio-frequency electrodes of the trap induces a.c. Stark shifts of the atomic transitions of the ions. The amplitude of the oscillating field experienced by the ions depends on the stray background static electric field. For our trap, we estimate that the stray electric field at the vicinity of the ions is ~ 5 V cm⁻¹. This produces a differential a.c. Stark shift between the $|\pm 1/2\rangle$ and $|\pm 5/2\rangle$ states to be ~ 120 mHz (ref. 34). The stray field is expected to be stable

at better than the 10^{-2} level during the course of the experiment, which translates to a change of less than 4 mHz in the oscillation frequency for the two-ion state.

Statistical analysis of the data. After each measurement block (Fig. 3b), we obtain a data point for the frequency difference between both states. We then bin the data points within 60 min intervals. The error bar for each binned data point is assigned using the calculated standard deviation within each bin. To extract the amplitudes of Lorentz violation, we perform a weighted least-squares fit of the binned data points to the model given in equation (4). We scale the 1 s.d. errors of the fitted parameters with $\sqrt{\chi^2_{\text{reduced}}} = 1.3$ to account conservatively for other remaining systematics.

Calculation of the energy shift due to the Lorentz-violation for $^{40}\text{Ca}^+$. Violations of Lorentz symmetry and Einstein's equivalence principle in bound electronic states result in a small shift of the Hamiltonian that can be described by⁹

$$\delta\mathcal{H} = -\left(C_0^{(0)} - \frac{2U}{3c^2}c'_{00}\right)\frac{\mathbf{p}^2}{2} - \frac{1}{6}C_0^{(2)}T_0^{(2)}$$

where we use atomic units, \mathbf{p} is the momentum of a bound electron, U is the Newtonian potential and c is the speed of light. The parameters $C_0^{(0)}$, $C_0^{(2)}$ and c'_{00} are elements of the $c'_{\mu\nu}$ tensor, which characterizes Lorentz violation. The relativistic form of the \mathbf{p}^2 operator is $c_{\gamma 0} \gamma^j p_j$ (a summation is implied by repeated indices), where γ^j are the Dirac gamma matrices. The non-relativistic form of the $T_0^{(2)}$ operator is $T_0^{(2)} = \mathbf{p}^2 - 3p_z^2$, where p_z is the component of the momentum along the quantization axis, and the relativistic form is $T_0^{(2)} = c_{\gamma 0} (\gamma^j p_j - 3\gamma^3 p_3)$. Therefore, the shift in the $\text{Ca}^+ 3d^2D_{5/2}$ energy level due to the $c'_{\mu\nu}$ tensor depends on the values of the $\langle 3d^2D_{5/2} | \mathbf{p}^2 | 3d^2D_{5/2} \rangle$ and $\langle 3d^2D_{5/2} | T_0^{(2)} | 3d^2D_{5/2} \rangle$ matrix elements.

Using the Wigner-Eckart theorem we express the matrix element of the irreducible tensor operator $T_0^{(2)}$ through the reduced matrix element $\langle J || T^{(2)} || J \rangle$ of the operator $T^{(2)}$ as

$$\langle J m_J | T_0^{(2)} | J m_J \rangle = \frac{-J(J+1) + 3m_J^2}{\sqrt{(2J+3)(J+1)(2J+1)(2J-1)}} \langle J || T^{(2)} || J \rangle \quad (6)$$

The expressions for the \mathbf{p}^2 and $T^{(2)}$ matrix elements are given in the supplementary material of ref. 9. The values of the angular factor in equation (6) (that is, the prefactor of the reduced matrix element) are $-0.27951 + 0.22361 m_J^2$ for $3d^2D_{3/2}$ and $-0.21348 + 0.073193 m_J^2$ for $3d^2D_{5/2}$.

First we calculated the required matrix elements in a lowest-order Dirac-Fock (DF) approximation and then with an additional random-phase approximation (DF+RPA). Next we carried out much more accurate calculations using the configuration interaction method with single and double excitations (CI+SD) and four variants of the all-order (linearized coupled-cluster) method³⁵. The virial theorem is also used for the \mathbf{p}^2 calculations.

The results are summarized in Extended Data Table 1. We note that we list the reduced matrix elements for the $T^{(2)}$ operator but actual matrix elements for the \mathbf{p}^2 operator because there is no necessity to introduce reduced matrix elements for a scalar operator. The values in columns DF(FC) and DF are lowest-order Dirac-Fock values calculated with and without the frozen-core approximation. In the frozen-core approximation the Dirac-Fock equations for the core electrons are solved self-consistently first and the valence orbital is calculated with an unchanged, that is, 'frozen', core. For the \mathbf{p}^2 operator such an approximation appears to give very poor results for the $3d$ states. If the core orbitals are allowed to vary together with the valence orbital, the lowest-order value differs by only 16% from the final virial theorem value. Addition of the RPA correction to the frozen-core Dirac-Fock value fixes this problem as well, because RPA corrections describe the reaction of the core electrons to an externally applied perturbation. The perturbation produced by the operator \mathbf{p}^2 is very large and, as a result, the RPA corrections for $\langle \psi | \mathbf{p}^2 | \psi \rangle$ matrix elements are large. Such a problem does not arise for the $T^{(2)}$ operator; the correlation correction to its matrix elements is much smaller and the accuracy of the resulting values is much higher.

The CI+SD calculations are carried out using the Dirac-Fock basis for the occupied core and valence atomic states and the Dirac-Fock-Sturm basis for unoccupied virtual orbitals; the frozen-core approximation is not used. The description of the Dirac-Fock-Sturm equations is given in refs 36, 37. The configuration state functions are constructed from the one-electron wavefunctions as a linear combination of Slater determinants. The set of the configuration state functions is generated including all single and double excitations into one-electron states of the positive spectrum. Single excitations are allowed to all core shells; double excitations are allowed to $3s$ and $3p$ core shells.

To calculate the value $\langle \psi | \mathbf{p}^2 | \psi \rangle$, where $|\psi\rangle$ is the valence electron wavefunction, we also used the approach based on the virial theorem. In the nonrelativistic limit the virial theorem can be written in the form

$$E = -\frac{1}{2} \langle \Psi | \sum_{i=1}^N \mathbf{p}^2(i) | \Psi \rangle$$

where E is the total energy of the system, N is the total number of electrons and $|\Psi\rangle$ is the total wavefunction of all electrons in the atom. Therefore, the value $\langle \psi | \mathbf{p}^2 | \psi \rangle$ can be calculated using the removal energies of the valence electron. The virial theorem makes it possible to calculate the expectation value of the \mathbf{p}^2 operator as twice the difference of the total energies E_N and E_{N-1} of N and $N-1$ systems. Because the differential energy E can be calculated with an accuracy much higher than the wavefunction Ψ , this approach is appropriate for the light atoms and ions where relativistic effects are negligible. The virial theorem results that use experimental data for the $3d$ removal energies from ref. 38 are listed in column VT in Extended Data Table 1.

We have also carried out the calculations of the $\langle \psi | \mathbf{p}^2 | \psi \rangle$ and $\langle \psi | T^{(2)} | \psi \rangle$ matrix elements using the all-order (linearized coupled-cluster) method³⁵. The all-order method gave very accurate values of the $3d_j$ lifetimes³⁹ and quadrupole moments⁴⁰ in a Ca^+ ion. In the all-order method, single, double and partial triple excitations of Dirac-Hartree-Fock wavefunctions are included to all orders of perturbation theory. We refer the reader to the review in ref. 35 for the description of the all-order method and its applications. Both single-double (SD) and single-double-partial-triple (SDPT) *ab initio* all-order calculations were carried out. In addition, a scaling of the dominant terms³⁵ was carried out for both SD and SDPT calculations to improve the accuracy and to evaluate the uncertainty of the final values. The calculations were carried out with both nonrelativistic and relativistic operators; the differences were found to be negligible at the present level of accuracy. The values calculated with relativistic operators are listed in Extended Data Table 1.

The virial theorem values are taken as final for the matrix element of the \mathbf{p}^2 operator. The uncertainty of 12% is estimated as the difference of the virial theorem and all-order values. The SD scaled values are taken as final for the $T^{(2)}$ operator (see refs 39, 40 for the discussion of the choice of the final all-order values). The uncertainty is determined as the spread of the four all-order values. On substituting the final all-order values of the $\langle 3d^2D_{5/2} | c_{\gamma 0} (\gamma^j p_j - 3\gamma^3 p_3) | 3d^2D_{5/2} \rangle$ matrix element into equation (6) and using the virial theorem value of $\langle 3d^2D_{5/2} | \mathbf{p}^2 | 3d^2D_{5/2} \rangle$, we get

$$\frac{\Delta E}{h} \approx \left(C_0^{(0)} - \frac{2U}{3c^2}c'_{00} \right) \times (-2.46 \times 10^{15} \text{ Hz}) + C_0^{(2)} \times (2.17 \times 10^{15} - 1.47 \times 10^{15} m_J^2) \text{ Hz}$$

for $3d^2D_{3/2}$, and

$$\frac{\Delta E}{h} \approx \left(C_0^{(0)} - \frac{2U}{3c^2}c'_{00} \right) \times (-2.46 \times 10^{15} \text{ Hz}) + C_0^{(2)} \times (2.16 \times 10^{15} - 7.42 \times 10^{14} m_J^2) \text{ Hz}$$

for $3d^2D_{5/2}$, where the uncertainties in the frequency coefficients of $\left(C_0^{(0)} - \frac{2U}{3c^2}c'_{00} \right)$ and $C_0^{(2)}$ are estimated to be 12% and 2%, respectively, and the atomic units are converted to SI units using $1 \text{ a.u.} \approx h \times (6.57968 \times 10^{15} \text{ Hz})$.

The frequency difference (in Hz) between the shifts of the $m_J = 5/2$ and $m_J = 1/2$ states for a pair of $^{40}\text{Ca}^+$ ions used in our experiment is given by

$$\frac{2}{h} (E_{m_J=5/2} - E_{m_J=1/2}) = (-1.484 \times 10^{15} \text{ Hz}) \times ((5/2)^2 - (1/2)^2) C_0^{(2)} = (-8.9(2) \times 10^{15} \text{ Hz}) \times C_0^{(2)}$$

Frame dependence of the $c'_{\mu\nu}$ tensor. Because of the Earth's motion, $c'_{\mu\nu}$ in the local laboratory frame varies according to the time-dependent Lorentz transformation given by

$$c'_{\mu\nu} = c_{MN} A_{\mu}^M A_{\nu}^N$$

where A is the Lorentz transformation matrix and $c'_{\mu\nu}$ is $c'_{\mu\nu}$ written in the Sun-centred, celestial-equatorial frame (SCCEF). The matrix A consists of a rotation and a velocity boost of the experiment with respect to the Sun. In the laboratory frame, we define the \hat{x} axis to point to the East, the \hat{y} axis to point to the North and the \hat{z} axis to point upward. The rotation matrix that transforms from the SCCEF to the local laboratory frame is given by

$$R = \begin{pmatrix} -\sin(\omega_{\oplus} T) & \cos(\omega_{\oplus} T) & 0 \\ -\cos(\chi) \cos(\omega_{\oplus} T) & -\cos(\chi) \sin(\omega_{\oplus} T) & \sin(\chi) \\ \sin(\chi) \cos(\omega_{\oplus} T) & \sin(\chi) \sin(\omega_{\oplus} T) & \cos(\chi) \end{pmatrix}$$

where the angle $\chi \approx 52.1^\circ$ is the colatitude of the experiment (Berkeley, California), T is time since the vernal equinox of 2014 and $\omega_{\oplus} = 2\pi/(23.93 \text{ h})$ is the sidereal

angular frequency of the Earth's rotation. The boost of the experiment in the SCCEF is given by

$$\beta = \begin{pmatrix} -\beta_{\oplus} \sin(\eta) \cos(\Omega T) \\ \beta_{\oplus} \cos(\eta) \cos(\Omega T) - \beta_L \sin(\chi) \cos(\omega_{\oplus} T) \\ -\beta_{\oplus} \sin(\Omega T) + \beta_L \sin(\chi) \sin(\omega_{\oplus} T) \end{pmatrix}$$

where $\beta_{\oplus} \approx 10^{-4}$ is the boost from the Earth's orbital velocity, $\beta_L \approx 1.5 \times 10^{-6}$ is the boost from the Earth's rotation, Ω is the yearly sidereal angular frequency and $\eta \approx 23.4^\circ$ is the angle between the ecliptic plane and the Earth's equatorial plane.

The parameter relevant to our experiment is $C_0^{(2)}$. With the Lorentz transformation applied to $c'_{\mu\nu}$ in the SCCEF, we can write the value of $C_0^{(2)}$ in the local laboratory frame in terms of $c'_{\mu\nu}$ in the SCCEF as

$$C_0^{(2)} = A + \sum_j (C_j \cos(\omega_j T) + S_j \sin(\omega_j T))$$

where the index j runs over all angular frequencies (ω_j) and the corresponding amplitudes (C_j, S_j) given in Extended Data Table 2, and A is a constant offset. For our 23 h measurement, the time-dependent Lorentz-violation signal is given at leading order by

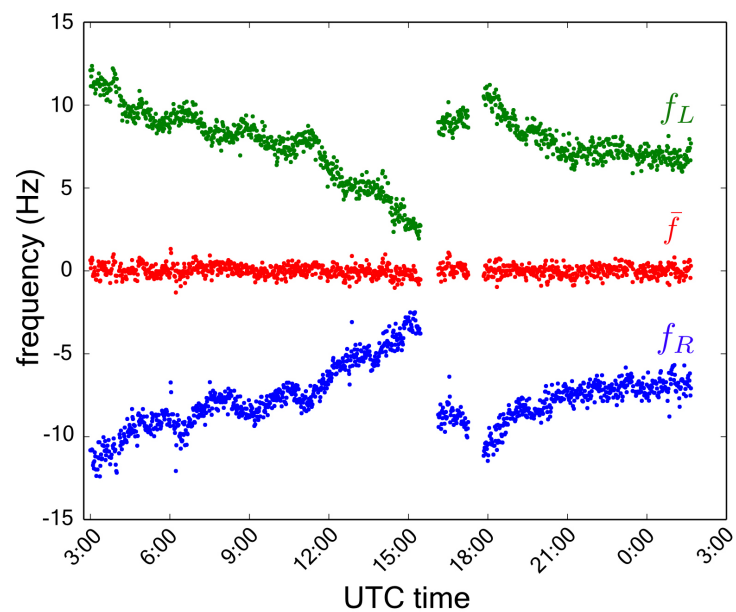
$$C_0^{(2)} = -3 \sin(2\chi) c'_{XZ} \cos(\omega_{\oplus} T) - 3 \sin(2\chi) c'_{YZ} \sin(\omega_{\oplus} T) \\ - \frac{3}{2} (c'_{XX} - c'_{YY}) \sin^2(\chi) \cos(2\omega_{\oplus} T) - 3 c'_{XY} \sin^2(\chi) \sin(2\omega_{\oplus} T)$$

We fit our binned 23 h measurement data to this model and extract Lorentz-violation parameters. In Table 1 we report uncorrelated combinations of parameters by diagonalizing the covariance matrix from the fit. We scale the 1 s.d. uncertainties

from the fit with $\sqrt{\chi^2_{\text{reduced}}} = 1.3$ to account conservatively for other remaining systematics.

With a year-long measurement, we expect to reach a sensitivity of 1 mHz in the ions' oscillation frequency. This level of sensitivity allows us to bound c'_{TX} , c'_{TY} and c'_{TZ} at the 10^{-16} level, which will improve the present limits^{9,41} on these parameters by at least an order of magnitude.

30. Wolf, P., Chapelet, F., Bize, S. & Clairon, A. Cold atom clock test of Lorentz invariance in the matter sector. *Phys. Rev. Lett.* **96**, 060801 (2006).
31. Kostelecký, V. A. & Mewes, M. Signals for Lorentz violation in electrodynamics. *Phys. Rev. D* **66**, 056005 (2002).
32. Bailey, Q. & Kostelecký, V. A. Lorentz-violating electrostatics and magnetostatics. *Phys. Rev. D* **70**, 076006 (2004).
33. Häffner, H. et al. Robust entanglement. *Appl. Phys. B* **81**, 151–153 (2005).
34. Yu, N., Zhao, X., Dehmelt, H. & Nagourney, W. Stark shift of a single barium ion and potential application to zero-point confinement in a rf trap. *Phys. Rev. A* **50**, 2738–2741 (1994).
35. Safronova, M. S. & Johnson, W. R. All-order methods for relativistic atomic structure calculations. *Adv. At. Mol. Opt. Phys.* **55**, 191–233 (2008).
36. Tupitsyn, I. I. et al. Magnetic-dipole transition probabilities in B-like and Be-like ions. *Phys. Rev. A* **72**, 062503 (2005).
37. Tupitsyn, I. I. et al. Relativistic calculations of the charge-transfer probabilities and cross sections for low-energy collisions of H-like ions with bare nuclei. *Phys. Rev. A* **82**, 042701 (2010).
38. Kramida, A. Ralchenko, Yu., Reader, J. & NIST ASD Team. *NIST Atomic Spectra Database (version 5.1)* <http://physics.nist.gov/asd> (NIST, 2013).
39. Kreuter, A. et al. Experimental and theoretical study of the $3d^2D$ -level lifetimes of $^{40}\text{Ca}^+$. *Phys. Rev. A* **71**, 032504 (2005).
40. Jiang, D., Arora, B. & Safronova, M. S. Electric quadrupole moments of metastable states of Ca^+ , Sr^+ , and Ba^+ . *Phys. Rev. A* **78**, 022514 (2008).
41. Altschul, B. Limits on Lorentz Violation from synchrotron and inverse Compton sources. *Phys. Rev. Lett.* **96**, 201101 (2006).



Extended Data Figure 1 | Cancellation of the contributions from the magnetic field gradient. The frequency measurements of the states $|\psi^L\rangle$ and $|\psi^R\rangle$ for a Ramsey duration of 100 ms are shown in the top green (f_L) and

bottom blue (f_R) data sets, respectively. We offset both data sets for visualization purposes. The contribution from the magnetic field gradient is subtracted out in the average frequency $\bar{f} = (f_L + f_R)/2$, which is shown as red data points.

Extended Data Table 1 | Lowest-order DF, DF+RPA, CI+SD and all-order results for the $\langle 3d^2D_J | p^2 | 3d^2D_J \rangle$ and $\langle 3d^2D_J || T^{(2)} || 3d^2D_J \rangle$ matrix elements in Ca^+ in atomic units

Matrix element	DF(FC)	DF	RPA	CI+SD	All-order	VT	Final
$\langle 3d^2D_{3/2} p^2 3d^2D_{3/2} \rangle$	3.05	0.67	0.66	0.73	0.83	0.748	0.75(9)
$\langle 3d^2D_{5/2} p^2 3d^2D_{5/2} \rangle$	3.04	0.66	0.66	0.73	0.83	0.748	0.75(9)
$\langle 3d^2D_{3/2} T^{(2)} 3d^2D_{3/2} \rangle$	5.45	6.22	5.72	6.89	7.09		7.09(12)
$\langle 3d^2D_{5/2} T^{(2)} 3d^2D_{5/2} \rangle$	7.12	8.11	7.47	8.98	9.25		9.25(15)

The virial theorem values are listed in column VT. The values in columns DF(FC) and DF are lowest-order Dirac–Fock values calculated with and without the frozen-core approximation.

Extended Data Table 2 | Amplitudes of various frequency components for $C_0^{(2)}$ expressed in terms of $c'_{\mu\nu}$ in the SCCEF

ω_j	C_j	S_j
ω_{\oplus}	$-3 \sin(2\chi)c'_{XZ} + 2c'_{TY}\beta_L$	$-3 \sin(2\chi)c'_{YZ} - 2c'_{TX}\beta_L$
$2\omega_{\oplus}$	$-\frac{3}{2}(c'_{XX} - c'_{YY}) \sin^2(\chi)$	$-3c'_{XY} \sin^2(\chi)$
Ω	$-\frac{1}{2}\beta_{\oplus}(3 \cos(2\chi) + 1)(c'_{TY} \cos(\eta) - 2c'_{TZ} \sin(\eta))$	$\frac{1}{2}\beta_{\oplus}c'_{TX}(3 \cos(2\chi) + 1)$
2Ω	0	0
$\Omega - \omega_{\oplus}$	$\frac{3}{2}\beta_{\oplus}c'_{TX} \sin(\eta) \sin(2\chi)$	$-\frac{3}{2}\beta_{\oplus} \sin(2\chi) (c'_{TY} \sin(\eta) + c'_{TZ}(1 + \cos(\eta)))$
$\Omega + \omega_{\oplus}$	$\frac{3}{2}\beta_{\oplus}c'_{TX} \sin(\eta) \sin(2\chi)$	$-\frac{3}{2}\beta_{\oplus} \sin(2\chi) (c'_{TZ}(1 - \cos(\eta)) - c'_{TY} \sin(\eta))$
$2\Omega - \omega_{\oplus}$	0	0
$2\Omega + \omega_{\oplus}$	0	0
$\Omega - 2\omega_{\oplus}$	$-3\beta_{\oplus}c'_{TY} \cos^2\left(\frac{\eta}{2}\right) \sin^2(\chi)$	$-3\beta_{\oplus}c'_{TX} \cos^2\left(\frac{\eta}{2}\right) \sin^2(\chi)$
$\Omega + 2\omega_{\oplus}$	$3\beta_{\oplus}c'_{TY} \sin^2\left(\frac{\eta}{2}\right) \sin^2(\chi)$	$-3\beta_{\oplus}c'_{TX} \sin^2\left(\frac{\eta}{2}\right) \sin^2(\chi)$
$2\Omega - 2\omega_{\oplus}$	0	0
$2\Omega + 2\omega_{\oplus}$	0	0

The frequencies ω_{\oplus} and Ω are the daily and yearly sidereal angular frequencies, respectively. The angle $\chi \approx 52.1^\circ$ is the colatitude of the experiment (Berkeley, California). The angle $\eta \approx 23.4^\circ$ is the angle between the plane of the ecliptic and the Earth's equatorial plane. $\beta_{\oplus} \approx 10^{-4}$ is the boost from the Earth's orbital velocity and $\beta_L \approx 1.5 \times 10^{-6}$ is the boost from the Earth's rotation. For our 23 h-measurement, contributions from these two boosts are negligible.